Frank-van der Merwe Growth in Bilayer Graphene

Haozhe Wang[1][†], Zhenpeng Yao[2][†], Wei Sun Leong[1], Gang Seob Jung[3], Qichen Song[4], Marek Hempel[1], Tomas Palacios[1], Gang Chen[4], Markus J. Buehler[3], Alán Aspuru-Guzik[2,5,6,7] and Jing Kong[1]*

[1]*Department of Electrical Engineering and Computer Science, Massachusetts Institute of Technology, Cambridge, MA 02139, USA*

[2]*Department of Chemistry and Chemical Biology, Harvard University, Cambridge, MA 02138, USA*

[3]*Department of Civil and Environment Engineering, Massachusetts Institute of Technology, Cambridge, MA 02139, USA*

[4]*Department of Mechanical Engineering, Massachusetts Institute of Technology, Cambridge, MA 02139, USA*

[5]*Department of Chemistry and Department of Computer Science, University of Toronto, Toronto, Ontario M5S 3H6, Canada*

[6]*Vector Institute for Artificial Intelligence, Toronto, Ontario M5S 1M1, Canada*

[7]*Canadian Institute for Advanced Research (CIFAR) Senior Fellow, Toronto, Ontario M5S 1M1, Canada*

*Corresponding author. Email: jingkong@mit.edu (J.K.)

[†]These authors contributed equally to this work.

Abstract

Bilayer graphene has attracted interest for its unique properties, including interesting electrical behavior when one layer is slightly rotated relative to the other. However, the quality of large-area bilayer graphene is often limited by the layer-plus-island growth mode in which islands of thicker graphene present as unavoidable impurities. Here, we report the observation of the layer-by-layer, Frank-van der Merwe (FM) growth mode in bilayer graphene where multilayer impurities are suppressed. Instead of the conventional surface adhesive energy, it is found that interface adhesive energy is possible to be tuned with an oxidative pretreatment. The FM-grown bilayer graphene is of AB-stacking or with small-twisting-angle ($\theta = 0\text{-}5°$), which is more mechanically robust compared to monolayer graphene, facilitating a free-standing wet transfer technology.

High-quality synthesis, systematic characterization and clean transfer of large-area bilayer graphene (2LG) are important for transforming the unusual physical properties of 2LG into disruptive technologies [1-3]. Specifically, small-twisting-angle 2LG ($\theta = 0 - 5°$) exhibits fascinating properties, including superconductivity [4-7] and electrically tunable bandgaps [8-10] compared to other 2LG with larger twisting angles [11]. Significant progress has been made with 2LG synthesis via controlling the cooling to let the dissolved carbon to precipitate out [12-14], or through the chemical vapor deposition (CVD) "pocket" approach [15]. Particularly, in the pocket method the most common observation is that the synthesis follow a Stranski–Krastanov (SK) mode [16,17], in which growth within a layer and nucleation of additional layers unavoidably occur at the same time. This method makes it unlikely that only 2LG forms uniformly over a large area as regions of single layer graphene (1LG) or other multilayers (3LG, 4LG, etc.) form.

We report uniform growth of 2LG using the Frank-van der Merwe (FM) growth mode in CVD graphene [16] using the pocket approach. In the FM mode, the existing layer continues to grow and merge into a film prior to the nucleation of an additional layer. This requires the energy nucleate a new layer (i.e., surface adhesive energy) is much larger than the energy to grow the existing layer (i.e., atomic cohesive energy). Previous studies found that the growth of additional graphene layers happens at the interface of the existing graphene layer and the Cu substrate instead of growing on top of the existing layer [15,18]. By tuning the interface adhesive energy, our calculations and experiments both show that the 3rdLG nucleation can be substantially suppressed in a 2LG film. Although a fully continuous 2LG film is not achieved in this study yet, the occurrence of graphene multilayers is substantially suppressed in the FM-mode-grown samples compared to that of SK mode.

Through first-principle calculations, the likelihood of an incoming carbon atom for 3rdLG nucleation *versus* to extend the 2ndLG growth at the interface of first layer of graphene (1stLG) and modified Cu were estimated (Fig. 1A). In the Cu growth substrate, we chose oxygen atoms as adatoms because they promote graphene growth with larger crystal sizes [19]. For comparison, we constructed a model with the same configuration, except that the Cu substrate is original and contains no adatoms (Fig. 1B) and determined the carbon atom formation energies at eight different locations (Fig. 1C). The atomic cohesive energies of 2LG are typically much smaller compared to the interface adhesive energies of 3LG nucleation. This relative difference implies that an incoming carbon atom should extend the 2LG growth, rather than nucleating the 3rd LG for both bare and modified Cu substrates. Compared to bare Cu, the interface adhesive energy required for 3LG nucleation on the modified Cu substrate (Cu_xO_{1-x}) is much higher (Fig. 1C, 1D). The ΔE of Cu_xO_{1-x} is twice that of the bare Cu (1.82 eV/C versus 3.73 eV/C), indicating that the incorporation of oxygen atoms on Cu surface can substantially suppress the 3LG nucleation. We can calculate the Boltzmann factor, which is the ratio of probabilities of two events (2ndLG growth versus 3rdLG nucleation), using:

$$\frac{\exp\left(-\frac{\Delta E_{F2} + \Delta E_{M2}}{k_B T}\right)}{\exp\left(-\frac{\Delta E_{F3} + \Delta E_{M3}}{k_B T}\right)} = \exp\left(-\frac{\Delta E_{F2} - \Delta E_{F3}}{k_B T}\right) \exp\left(-\frac{\Delta E_{M2} - \Delta E_{M3}}{k_B T}\right) \tag{eq. 1}$$

where ΔE_{Fi} (Fig. 1C) and ΔE_{Mi} are the formation energy and migration barrier of an incoming carbon atom attaches to the i_{th} layer of graphene, respectively, k_B is the Boltzmann constant, and T is the growth temperature (*i.e.* 1050

°C). Assuming the 3LG nucleation requires no further interface diffusion, $\Delta E_{M3} \sim 0$, and the reported activation energy for a C atom to perform both bulk and interface diffusion, ΔE_{M2} is 1.42 eV [10], the Boltzmann factor of 2LG growth versus 3LG nucleation on pure and modified Cu substrates are $3.2 \times 10_1$ and $7.1 \times 10_8$, respectively. This implies that if we have a 2LG film of 1 cm2 size, the maximum area that the 3LG can grow at the 2LG/substrate interface for both Cu and Cu$_x$O$_{1-x}$ are 3.1 mm2 and 0.14 µm2, respectively (19). This suggests that centimeter-scale, high-purity 2LG film can be realized by tuning the interface adhesive energy.

We implemented this strategy by using a mild oxidation pretreatment step integrated into the CVD "pocket" approach (Fig. 1E)(19). For comparison, the same growth steps are carried out for both bare and treated Cu foil. For graphene samples synthesized on bare Cu, we observed random growth of 3LG islands and inevitable nucleation of thicker layers, similar to previous reports [18,20]. For graphene samples synthesized on treated Cu, we observed no 3LG impurities (Fig. 1E). We only saw 1LG and 2LG regions under an optical microscope over an area of 2 cm2. We performed the same comparison studies on two types of commercial Cu foils (Alfa Aesar 13380 and 46986; Fig. 1F) and observed successful suppression of the 3LG nucleation, indicating that this mechanism is not limited to the specific types of Cu foils. In addition, we conducted a series of surface analyses on the treated Cu and found that our pre-treatment modifies the surface stoichiometry of a bare Cu to CuO$_{1.7}$. This surface-level oxidation disappears after 720 s of argon ion sputtering in an X-ray photoelectron spectroscopy (Fig. S1).

In the current study, galaxy-like 2LG morphologies were obtained at the centimeter-scale 1$_{st}$LG/Cu interface.. Over a 1 x 1 mm2 optical imaging area, we observed merging of 2LG domains into an elliptical film surrounded by numerous 2LG sparse domains and 1LG regions (Fig. 1H). Similar graphene ad-layer morphologies were observed regardless of whether the Cu was treated (Fig. S2). We attributed this galaxy-like growth morphology to the sparse locations of bulk diffusion of carbon atoms (*i.e.* from Cu interior to exterior through the foil thickness), and the limited interface-diffusion length of carbon atoms at the 1$_{st}$LG/Cu interface [21], corresponding to Steps (ii) and (iii) in Fig. 1G (19). Bulk diffusion may happen via preferred paths, due to the presence of uncontrollable impurities in the commercial Cu foil [22]. Carbon atoms that penetrated through bulk Cu will emerge at several preferred points within the Cu surface lattice and start to migrate via interface diffusion. According to diffusion theories, carbon concentration surrounding a penetration point follows Gaussian distributions [23]. Engineering of the treated Cu to provide increased bulk diffusion paths should increase the area coverage of 2LG.

We statistically analyzed the SK and FM-mode-grown samples using optical microscopy (Fig. 2A, C). On the bare Cu substrate, the SK growth mode appears to be dominant (Fig. 2A, 2B). We found 2LG domains using the SK growth mode with an average size of ~10 µm, but multi-layer impurities appear even when the growth is limited to one hour. As the growth duration increased from 1h to 4 h, bilayer graphene domains get larger in size and eventually merge into a film. However, these are accompanied by not only the concurrent growth of 3LG and 4LG impurities, but also the nucleation of subsequent layers up to 8LG. In contrast, when we used treated Cu for one hour, most of the 2LG domains synthesized on the treated Cu substrate of regular hexagonal shape (Fig. 2C). The domain size of the 2LG increased with growth duration, and we observed no 3LG nucleation of 3LG for up to three hours (Fig. 2C, D). Our typical 3 h-grown sample had connection of 2LG domains into a larger film with merging

slit widths smaller than 1 µm. We observe the appearance of a µm-sized 3LG domain in a 2LG continuous region for our typical 4 h-grown samples, but without any 4LG impurities (Fig. 2C).

To quantitively evaluate the suppression of multilayer impurities in our FM-mode-grown bilayer graphene film, we developed a statistical method with the help of microscopy analysis. Specifically, we first converted the original microscopy images of graphene films transferred on Si/SiO$_2$ substrates into grayscale and plotted the corresponding pixel counts (5,002,624 pixels for each image). A histogram for a typical FM-mode grown graphene grown for one hour contains only two peaks (1LG and 2LG), while that of SK-mode contains four peaks, which can be attributed to 1LG, 2LG, 3LG and 4LG (Fig. 2E). To systematically label graphene region with different layer numbers, we assigned a range of gray levels to each histogram peak and converted the corresponding pixels into red (Fig. 2E). Upon layer labelling in each microscopy image, we estimated the occurrence probability of 2LG and multilayer impurities by extracting the ratio of pixel counts. For this analysis (Fig. 2F), all samples were grown for 3.33 h. We randomly acquired a 10 microscopy images, with sizes of at most 40×40 µm$_2$, from both the SK- and the FM-mode grown graphene samples (Fig. 2F). The occurrence probability of 2LG is less than half (46.20 ± 14.22%) for the SK-mode grown samples, while that of FM-mode is close to 100% (99.32 ± 0.34%).

We found using Raman spectroscopy that our FM-mode grown bilayer graphene are quasi-AB stacked (i.e., either AB-stacked or having a small twisting angle (θ = 0-5°))(Fig. 3A) [24,25]. A typical 1LG Raman signature is shown in Fig 3A, spot 1 with the positions of G and 2D bands (ω_G and ω_{2D}) located at 1582 and 2670 cm$_{-1}$, respectively. The intensity ratio of 2D to G bands (I$_{2D}$/I$_G$) is ~2, and the 2D full width at half maximum (Γ_{2D}) is 34 cm$_{-1}$. The other spots exhibited an almost identical Raman spectra with ω_G = 1580 cm$_{-1}$, ω_{2D} = 2680 cm$_{-1}$, I$_{2D}$/I$_G$ = ~1, and Γ_{2D} = 58 cm$_{-1}$. These features all can be identified as 2LG with either AB-stacked or small twisting angles (θ = 0 - 5°) [24,25]. We obtained consistent results from 60 different Raman spectra, that we randomly collected from 6 different samples, confirming our growth method produces quasi-AB stacked 2LG. In contrast, for the SK-mode grown graphene sample (Fig. 3B), the Raman spectra taken at 4 typical spots all had different ω_G, ω_{2D}, I$_{2D}$/I$_G$, and Γ_{2D}. We identified the Raman spectra of spots 1 and 4 in Fig. 3B 1LG and 3LG, respectively. Under the optical microscope, we recognized spots 2 and 3 as 2LG because they shared the same optical contrast, which is at the interval of 1LG and 3LG (Fig. 3B). One spot was 2LG with a small-twisting-angle (I$_{2D}$/I$_G$ = 0.77 and Γ_{2D} = 62 cm$_{-1}$) and the other had a larger-twisting-angle 2LG (I$_{2D}$/I$_G$ = 2.3 and Γ_{2D} = 37 cm$_{-1}$) [23]. The variation of twisting angles in the SK-mode-grown 2LG is large, unlike those in the FM-mode.

We also performed Raman mappings on both FM- and SK-mode-grown graphene samples that we transferred onto Si/SiO$_2$. For the FM-mode sample, we collected a total of 18,000 Raman spectra across a selected area of 30×24 µm$_2$, which consisted of two 2LG domains that merged and were encompassed by 1LG region. We found the I$_{2D}$/I$_G$ constantly remains as ~1.0 throughout the two merging domains of 2LG (Fig. 3C). We collected a total of 20,250 Raman spectra from a typical SK-mode sample, over an area that consists of 1LG, 2LG, 3LG, and multilayer graphene (MLG) (Fig. 3C). Surprisingly, we classified the 2LG region, which looks uniform under optical microscope, into at least 2 divisions in the Raman map of I$_{2D}$/I$_G$ (Fig. 3F). We further classified these Raman mapping data using a simple and fast unsupervised learning approach, the k-means algorithm, which measures dissimilarity between two data points using square Euclidean distance (19). We considered all 5 parameters (ω_G,

ω_{2D}, I2D, IG, and Γ_{2D}) in our artificial-intelligence-assisted Raman data classification. To visualize the classification results, we selected 3 parameters (ω_G, ω_{2D}, and Γ_{2D}) and made three-dimensional plots (Fig. 3D, E). The algorithm clustered all 18,000 Raman spectra into two classes in several seconds. By reading the mean value ($\overline{\omega_G}$, $\overline{\omega_{2D}}$, $\overline{\Gamma_{2D}}$) of each cluster, we identified Class I and II as the Raman data of 1LG and quasi-AB-stacked 2LG, respectively. Error rate of our AI-assisted Raman analysis is 0.027, as cross-verified by hierarchical clustering algorithm. By manually verifying the Raman data at the boundary between Class I and II in Fig. 3E, we found that these data were collected along the 2LG edges (Fig. 3C & S3). This is understandable that Raman spectra collected near the 2LG edges have contributions from both 1LG and 2LG regions as our laser spot size was ~500 nm and the mapping step size was 200 nm. We executed the same algorithm for comparison on the Raman data of SK-mode sample (Fig. 3G and H), where Class I to V in Fig. 3H represents 1LG, quasi-AB-stacked 2LG, larger-twisting-angle 2LG, 3LG, and MLG, respectively. Using the artificial-intelligence-assigned class number (I to V), we constructed a spatial map (Fig. S4), where the boundaries/edges that separate 1LG, 2LG, and 3LG *etc.* can be recognized. For graphene samples on substrates without a good optical contrast such as glass, quartz or sapphire, the Raman mapping (e.g. Fig. 3F lower panel) or this facile classification method will be very useful to identify regions of different stacking orders and layer numbers.

Utilizing the mechanical advantage of 2LG in comparison to 1LG [26], we devised a support-free wet transfer approach driven by Marangoni effect. Owing to graphene's thinness, a transfer support layer is generally required to prevent cracks' generation and propagation. In the conventional polymer-supported CVD graphene transfers [27,28], a polymer sacrificial support layer was first coated on a piece of graphene/Cu. The coated sample was then floated on an etchant solution to completely remove the Cu. The sample was then rinsed with deionized water for at least three times. For these rinsing steps, a flat scoop (*e.g.,* Si wafer or glass slide) was used to move the sample from one beaker of deionized water to another, and an external force (*i.e.,* tweezers or glass slide) was required to drive the sample from liquid surface to the flat scoop, until the sample is free of Cu etchant residues. If these rinsing steps were carried out without the polymer support layer, the external force usually generates cracks and tears in the graphene layer. To eliminate the need of sacrificial transfer support layer, we substitute the external force with Marangoni-driven internal forces, which are the hydrodynamic forces generated whenever liquids with different surface tensions mix [29]. To achieve these, prior to sample loading, we fine-tuned the liquids' surface tension with the help of isopropyl alcohol (IPA). We first wetted a flat scoop with a liquid of higher surface tension (high-$\boldsymbol{\sigma}$), and quickly dipped it into the lower-surface-tension liquid with a floating graphene sample. Forced by Marangoni flows, the sample will automatically climb from liquid surface to the flat scoop, in a few seconds (Movie S1). When we gently dipped the flat scoop back into the high-$\boldsymbol{\sigma}$ liquid, the graphene sample gradually glides to the liquid surface (19). Fig. 4D shows a typical image of a centimeter-scale 2LG sample transferred on Si/SiO2 substrate, using our free-standing Marangoni-driven graphene transfer process. We found the yield (in terms of area percentage for un-broken regions) of this transfer approach for our 2LG is > 95%, whereas for 1LG is ~ 66.7% (Fig. S5; Movie S2). This observation was consistent with our molecular dynamic simulations, AB-stacked 2LG was found to be robust under the Marangoni flow, even in the presence of atomic defects (Fig. 4B and C; Movie S3). A frame made by Scotch tape or silver paste was made on the surface of graphene outlining the four edges for

bootstrapping the area in our method, similar to the marker frame transfer approach [30], though the Marangoni effect simplify the transfer process and avoid using a dedicated experimental setup to exchange the etching/rinsing solution.. We anticipate this polymer-free, Marangoni-flow-driven transfer approach developed on our FM-mode-grown 2LG can be generalized to other few-layer 2D materials.

Methods

Cu substrate pre-treatment and bilayer graphene growth: Cu foil purchased from Alfa Aesar (#46365) with 25 μm thickness and 99.8% purity was used as the growth substrate in this work. Prior to growth, the Cu substrate was first subjected to a Ni etchant (Nickel Etchant TFB, Transense) to remove surface contaminations. To enable Frank-van der Merwe (FM) growth mode, the substrate was then annealed in ambient conditions at 130 °C for 3 h. We note that this step was omitted for all SK-mode grown samples. After substrate pre-treatment, the Cu foils were folded into a pocket, as discussed in previous work[31], and loaded into a low-pressure chemical vapor deposition (LPCVD) system. Temperature of the LPCVD system was then ramped up 1050 °C in 30 min (50 mTorr). In the next 30 min, the LPCVD system was maintained at 1050 °C. Following which, 50 sccm of H2 gas was introduced to the system, and 1 min later, 1 sccm of CH4 was added to the system to activate the growth of 2LG. The system was maintained at the same conditions until a desired growth duration ends (e.g., 3.33 h). We note all graphene in this work were grown using Cu foil purchased from Alfa Aesar (#46365), except for those shown Fig. 1F and S4. For Alfa Aesar Cu foil (#13380) with 127 μm thickness and 99.9% purity, we observe small arbitrary shapes bilayer graphene growth and successful suppression of additional graphene layers (Fig. 1F). For Alfa Aesar Cu foil (#46986) with 25 μm thickness and 99.8% purity, we observe no evidence of bilayer graphene growth (Fig. S6), which could be due to the difficulty of bulk diffusion [31].

PMMA-assisted graphene transfer: Notably, 2LG is synthesized at the exterior side of a Cu pocket, using the LPCVD approach described above. To transfer the 2LG from growth substrate to a destination substrate, the Cu pocket was carefully cut, with extra care given to the exterior side of Cu pocket. All samples characterized in this work were transferred on Si/SiO2 substrates with the help of polymethylmethacrylate (PMMA) support layers, unless otherwise specified. In the PMMA-supported graphene transfer, a 300 nm-thick layer of PMMA 950 A5 (Microchem Inc.) was first spun-coated on the graphene/Cu sample followed by a one hour of 80 °C oven baking. To remove the Cu growth substrate, the sample was then floated on top of Cu etchant (Copper Etchant TFB, Transense) for half an hour. Following which, the sample was rinsed with deionized water for at least thrice. For these steps of sample rinsing, a flat scoop (*i.e.,* Si wafer or glass slide) is used to ship the sample from one beaker of deionized water to another, and an external force (*i.e.,* tweezers) is required to drive the sample from liquid surface to the flat scoop, until the sample is free of Cu etchant residues. Finally, the destination substrate (*i.e.,* Si/SiO2 substrate) was used to fish the graphene film. To expedite sample drying, the sample was initially blew-dry with nitrogen flow, followed by an 8 h of 80 °C oven baking. To remove the sacrificial PMMA support layer, the sample must be then soaked in acetone for 6 h, rinsed with IPA, and finally blew dry with nitrogen.

Support-free Marangoni-driven graphene transfer: Similar to PMMA-assisted transfer, Cu pocket was first opened to obtain the 2LG grown at the exterior side. Silver paint (PELCO. Inc) or Scotch tape was then used to make a frame surrounding the region of interest, such that the operator can locate borders of the diced sample. Subsequently, the support-free 2LG sample was floated on top of the Cu etchant for 30 min to etch off the Cu substrate. In the subsequent rinsing process, the flat scoop was made more hydrophilic with an oxygen plasma treatment and the surface tension of deionized water was tuned by diluting with different amount of Isopropyl Alcohol (IPA). Specifically, a feasible combination of IPA concentrations is 15%, 5%, 2%, 1.5%, 1%, and 0%. The support-free graphene sample was initially shipped from a solution with the least surface tension (*i.e.,* 15% IPA) to another solution with the second-lowest surface tension (*i.e.,* 5% IPA), and so on, until the desired rinsing results achieved. At the last rinsing step, a destination substrate was pre-wetted with pure water (highest surface tension) and dipped into the solution with second-largest-surface-tension, which graphene sample is floating on it. Graphene sample will automatically climb onto the destination substrate, as schematically illustrated in Fig. 4A. For sample drying, blow dry is not recommended, and to expedite the process, an 8 h of 80 °C oven baking can be performed. The sample (*i.e.,* 2LG transferred on Si/SiO$_2$ substrate) is now ready to use.

Materials Characterization: A 532 nm excitation laser with a 100 ×objective lens in WITec Alpha 300 micro-Raman imaging system was used for acquisition of all Raman spectra and maps in this work. Field-emission scanning electron microscopy was conducted using a Zeiss Merlin High-resolution SEM. The X-Ray Photoelectron Spectroscopy was performed by Physical Electronics Versaprobe II X-ray Photoelectron Spectrometer.

First-Principle Calculations: The calculations were performed using the Vienna Ab-initio Simulation Package (VASP) [32,33] within the projector augmented wave (PAW) [34] formalism and the Perdew-Becke-Ernzerhof (PBE) [35] approximation to the exchange-correlation potential was employed. We used a plane wave basis with a cutoff energy of 520 eV and gamma-centered k-meshes, with a density of 8000 k-points per reciprocal atom. We also adopted the vdW-DF functional (optB88) [36], which employs a self-consistent van der Waals (vdW) correction. To simulate the nucleation and growth of graphene on the copper surface, we built a surface model with a 4" × 4" Cu (111) surface of 6 layers with a vacuum spacing of 15 Å and the bottom layer is fixed in the perpendicular direction to the surface (Fig. S7A) following the previous study[31]. To simulate the surface pretreatment, a similar oxidized Cu (111) surface model was built with Cu/O atomic configurations reproducing the counterpart in Cu$_2$O (Fig. S7A). Addition of the O ions to the system led to two geometrically different ways to introduce graphene to the oxidized surface (Fig. S7B). Both configurations were relaxed in density functional theory (DFT) with the one with lower total energy (O locates in the graphene ring center) chosen to be the configuration of the first graphene layer (1$_{st}$LG). Additions of the 2$_{nd}$ and 3$_{rd}$LG proceeded in an A-B stacking manner (Fig. S9).

Artificial Intelligence Data Analysis: We applied *k*-means clustering to separate unlabeled data samples into *k* groups with square Euclidean distance as a dissimilarity measure between two data points. In this unsupervised learning algorithm, all data points were clustered based on similarity. In another words, dissimilarity was minimized within each cluster. Specifically, dissimilarity between any data point and a cluster center is the distance from the

data point to the cluster center. Therefore, the dissimilarity within a cluster will be the sum over the distances between data points in that cluster and the cluster center. Summation of all cluster dissimilarities is called global dissimilarity, which can be calculated by iterating over each cluster, over each data point within the cluster, and over each feature of the data point:

$$\sum_{k=1}^{K} \sum_{n:X_n \in S_k} \sum_{d=1}^{D} (x_{n,d} - \mu_{k,d})^2$$

where k is the number of cluster, n is the number of data point, d is the number of feature, and $\mu_{k,d}$ is the mean of the cluster. Since we do not know the cluster centers of Raman data in advance, we initialize them with a set of values randomly picked from the existing data points. Subsequently, two steps were performed alternately: (i) assign each data point to the cluster with the closest cluster center, and (ii) update the cluster center to be the mean of all the data points in its cluster. Iteration of these two steps continues until a convergence point found. We note that k-means function from scikit-learn package was used in this work.

Molecular Dynamics Simulations: The molecular dynamics (MD) simulations in this study were performed using a LAMMPS [37] package. We utilized an Adaptive Intermolecular Reactive Empirical Bond Order (AIREBO) [38,39] potential to model the interaction between carbon atoms. The potential is an extended version of the Brenner's Reactive Empirical Bond Order (REBO) potential of the hydrocarbon system [38], which only could describe the short-range interaction (r < 2Å). Stuart *et al.* have expanded REBO by including the four bodies torsional term and Lennard-Jones (LJ) potential based van der Waals (vdW) terms [39], which describe layer-to-layer interaction in a bilayer graphene system. Instead of utilizing the original form of AIREBO, the radius cutoff of the switching function of C-C interaction is set to 2Å for both R_{min} and R_{max}, to describe failure behaviors, by completely turning off the stiffening effect from the switching function. The choice of cutoffs can successfully describe complex carbon network including pristine graphene without stiffening near the failure point [40]. Fig. S11 A and B show the monolayer and bilayer graphene models used for the MD simulations. The size of each graphene model is 40×40 nm[2]. The bilayer graphene is of AB-stacking, and the interlayer distance was set to 3.4 Å. By setting the atomic resolution to describe the bond breaking of graphene and vdW interactions between the layers as invariable, we implicitly handle the mass transport of mixed liquid due to Maragoni effect on the liquid surface as a part of spherical droplet exposed on the flat liquid surface by utilizing a moving spherical indenter. We approximate the hardness of the droplet using a simple equation for a spherical particle on the liquid surface [41] in Fig. S11C. From the small deformation, d, on the liquid surface due to the spherical solid, we obtain a linear relation from the vertical component of the surface tension on a spherical particle, $F = 2\pi R \gamma \sin^2 \theta$, by applying the approximation, $\sin^2 \theta \sim \frac{2d}{R}$,

$$F = 4\pi\gamma d,$$

where the γ is surface tension of liquid. The surface tension of water is typically 72 dynes/cm (~0.0078eV/Å) at 293 K[42]. In simulations, we set the linear spring for spherical indenter, k to ~ 0.005 eV/Å, as the mixture with alcohol reduces the surface tension.

We further assume that the graphene is initially contacted with the relatively flat liquid surface. The liquid surface is also implicitly described by Lennard Jones (LJ) wall as

$$E = \varepsilon \left[\frac{2}{15} \left(\frac{\sigma}{r} \right)^9 - \left(\frac{\sigma}{r} \right)^3 \right],$$

where the LJ parameters are obtained from previous graphene and water interface study [43] by using the mixing rule as $\varepsilon = 0.06$ eV, and $\sigma = 3.2$ Å with $r_{cut} = 3\sigma$. We restricted the movement of boundaries in the z-direction. After we relaxed the systems with NVT ensemble at 300 K for 20 ps using energy minimization principle, a sphere indenter with $R = 5$ nm moves with a speed 0.2 Å/ps (20 m/s) along the y direction, as shown in Fig. S11D. The center of the sphere is located under the water surface with a 10 nm distance.

REFERENCES AND NOTES

1   Ohta, T., Bostwick, A., Seyller, T., Horn, K. & Rotenberg, E. Controlling the electronic structure of bilayer graphene. *Science* **313**, 951-954 (2006).

2   Mayorov, A. *et al.* Interaction-driven spectrum reconstruction in bilayer graphene. *Science* **333**, 860-863 (2011).

3   Gao, Y. *et al.* Ultrahard carbon film from epitaxial two-layer graphene. *Nature nanotechnology* **13**, 133 (2018).

4   Yankowitz, M. *et al.* Tuning superconductivity in twisted bilayer graphene. *Science* **363**, 1059-1064 (2019).

5   Cao, Y. *et al.* Unconventional superconductivity in magic-angle graphene superlattices. *Nature* **556**, 43 (2018).

6   Codecido, E. *et al.* Correlated insulating and superconducting states in twisted bilayer graphene below the magic angle. **5**, *Science Advances* (2019).

7   Sharpe, A. L. *et al.* Emergent ferromagnetism near three-quarters filling in twisted bilayer graphene. **365**, 605-608, *Science* (2019).

8   Zhang, Y. *et al.* Direct observation of a widely tunable bandgap in bilayer graphene. *Nature* **459**, 820 (2009).

9   Tang, T.-T. *et al.* A tunable phonon–exciton Fano system in bilayer graphene. *Nature nanotechnology* **5**, 32 (2010).

10   Zhou, S. Y. *et al.* Substrate-induced bandgap opening in epitaxial graphene. *Nature materials* **6**, 770 (2007).

11   Zhang, J. & Zhao, J. Mechanical properties of bilayer graphene with twist and grain boundaries. *Journal of Applied Physics* **113**, 043514 (2013).

12   Ma, W. *et al.* Interlayer epitaxy of wafer-scale high-quality uniform AB-stacked bilayer graphene films on liquid Pt 3 Si/solid Pt. *Nature Communications* **10**, 2809 (2019).

13   Reina, A. *et al.* Growth of large-area single-and bi-layer graphene by controlled carbon precipitation on polycrystalline Ni surfaces. *Nano Research* **2**, 509-516 (2009).

14   Wu, Y. *et al.* Growth mechanism and controlled synthesis of AB-stacked bilayer graphene on Cu–Ni alloy foils. *ACS Nano* **6**, 7731-7738 (2012).

15   Hao, Y. *et al.* Oxygen-activated growth and bandgap tunability of large single-crystal bilayer graphene. **11**, *Nature Nanotechnology* 426 (2016).

16   Humphreys, C. Controlling crystal growth. *Nature* **341**, 689-689 (1989).

17   Gurioli, M., Wang, Z., Rastelli, A., Kuroda, T. & Sanguinetti, S. Droplet epitaxy of semiconductor nanostructures for quantum photonic devices. *Nature materials*, 1 (2019).

18   Fang, W. *et al.* Asymmetric growth of bilayer graphene on copper enclosures using low-pressure chemical vapor deposition. *ACS Nano* **8**, 6491-6499 (2014).

19   Hao, Y. *et al.* The role of surface oxygen in the growth of large single-crystal graphene on copper. *Science* **342**, 720-723 (2013).

20   Ta, H. Q. *et al.* Stranski–Krastanov and Volmer–Weber CVD growth regimes to control the stacking order in bilayer graphene. *Nano letters* **16**, 6403-6410 (2016).

21   Yoon, T. *et al.* Direct measurement of adhesion energy of monolayer graphene as-grown on copper and its application to renewable transfer process. *Nano Letters* **12**, 1448-1452 (2012).

22   Li, X., Colombo, L. & Ruoff, R. S. Synthesis of graphene films on copper foils by chemical vapor deposition. *Advanced Materials* **28**, 6247-6252 (2016).

23   Crank, J. *The mathematics of diffusion*. (Oxford university press, 1979).

24   Zhou, H. *et al.* Chemical vapour deposition growth of large single crystals of monolayer and bilayer graphene. *Nature Communications* **4**, 2096 (2013).

25   Kim, K. *et al.* Raman spectroscopy study of rotated double-layer graphene: misorientation-angle dependence of electronic structure. *Physical Review Letters* **108**, 246103 (2012).

26   Papageorgiou, D. G., Kinloch, I. A. & Young, R. Mechanical properties of graphene and graphene-based nanocomposites. *Progress in Materials Science* **90**, 75-127 (2017).

27   Leong, W. S. *et al.* Paraffin-enabled graphene transfer. *Nature Communications* **10**, 867 (2019).

28   Wang, H. *et al.* Low-temperature copper bonding strategy with graphene interlayer. *ACS nano* **12**, 2395-2402 (2018).

29   MacKay, G. & Mason, S. The Marangoni Effect and Liquid/Liquid Coalescence. *Nature* **191**, 488 (1961).

30   Pasternak, I. *et al.* Graphene films transfer using marker-frame method. *Aip Advances* **4**, 097133 (2014).

31   Hao, Y. *et al.* Oxygen-activated growth and bandgap tunability of large single-crystal bilayer graphene. *Nature Nanotechnology* **11**, 426 (2016).

32   Kresse, G. & Hafner, J. Ab initio molecular dynamics for liquid metals. *Physical Review B* **47**, 558 (1993).

33   Kresse, G. & Hafner, J. Ab initio molecular-dynamics simulation of the liquid-metal–amorphous-semiconductor transition in germanium. *Physical Review B* **49**, 14251 (1994).

34   Blöchl, P. E. Projector augmented-wave method. *Physical review B* **50**, 17953 (1994).

35   Perdew, J. P., Ernzerhof, M. & Burke, K. Rationale for mixing exact exchange with density functional approximations. *The Journal of chemical physics* **105**, 9982-9985 (1996).

36   Thonhauser, T. *et al.* Van der Waals density functional: Self-consistent potential and the nature of the van der Waals bond. *Physical Review B* **76**, 125112 (2007).

37   Plimpton, S. Fast parallel algorithms for short-range molecular dynamics. *Journal of computational physics* **117**, 1-19 (1995).

38   Brenner, D. W. *et al.* A second-generation reactive empirical bond order (REBO) potential energy expression for hydrocarbons. *Journal of Physics: Condensed Matter* **14**, 783 (2002).

39   Stuart, S. J., Tutein, A. B. & Harrison, J. A. A reactive potential for hydrocarbons with intermolecular interactions. *The Journal of chemical physics* **112**, 6472-6486 (2000).

40   Jung, G. S. & Buehler, M. J. Multiscale mechanics of triply periodic minimal surfaces of three-dimensional graphene foams. *Nano Letters* **18**, 4845-4853 (2018).

41   Rapacchietta, A. & Neumann, A. Force and free-energy analyses of small particles at fluid interfaces: II. Spheres. *Journal of Colloid Interface Science* **59**, 555-567 (1977).

42   Vargaftik, N., Volkov, B. & Voljak, L. International tables of the surface tension of water. *Journal of Physical Chemical Reference Data* **12**, 817-820 (1983).

43   Zhou, H. *et al.* Understanding controls on interfacial wetting at epitaxial graphene: Experiment and theory. *Physical Review B* **85**, 035406 (2012).
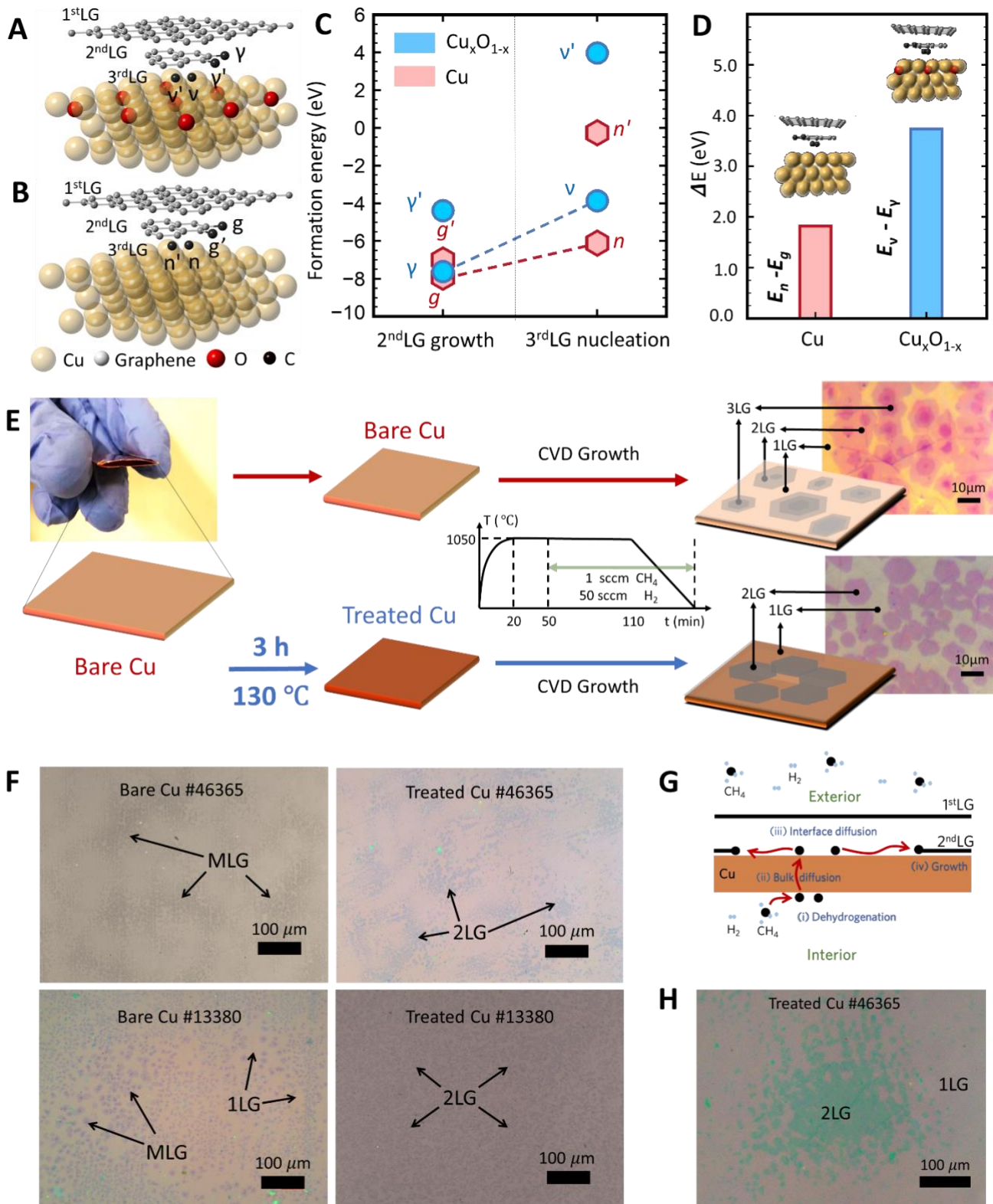
ACKNOWLEDGEMENTS

Fig. 1. Our Frank-van der Merwe (FM) mode-enabled bilayer graphene (2LG) growth. (**A** and **B**) Atomic geometries of the 2LG growth behavior on (**A**) pure and (**B**) modified Cu substrates. (**C**) Formation energies of the 2_{nd} layer graphene (2_{nd}LG) growth and the 3_{rd} layer graphene (3_{rd}LG) nucleation, on pure and modified Cu, respectively. (**D**) Energy difference, ΔE, correspond to suppression of the 3_{rd}LG nucleation for both pure and modified Cu. (**E**) Schematics showing the chemical vapor deposition (CVD) of 2LG on bare and treated Cu. (**F**)

13

Optical images of 2LG samples transferred on separate SiO$_2$/Si substrates, grown using different types of Cu foils as indicated. 1LG, 2LG and multilayer graphene (MLG) regions are labeled. These samples were grown for 1h. (**G**) Schematic illustrating the 2LG growth mechanism in the CVD Cu "pocket" approach. (**H**) Typical optical image of a 2LG sample transferred on a SiO$_2$/Si substrate, grown for 3.33h with the treated Cu, showing galaxy-like morphologies of 2LG.
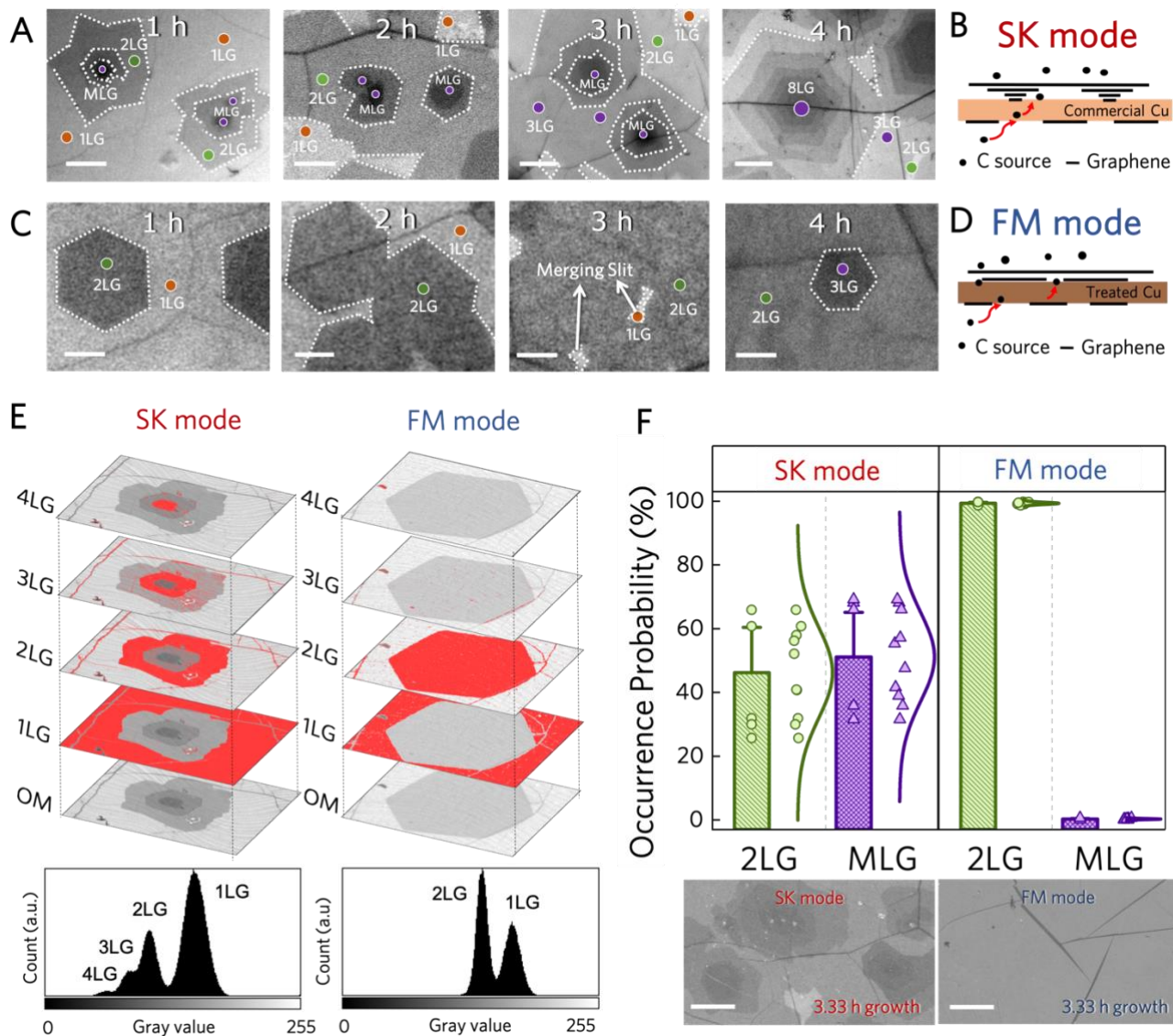
Fig. 2. Comparison of SK- and FM-mode grown 2LG films. (**A** and **C**) Optical images of graphene synthesized on (**A**) commercial Cu and (**C**) pre-treated Cu (cut from the same piece of commercial Cu foil in (A)), respectively, for different growth durations as indicated (*i.e.* 1 h, 2 h, 3 h, and 4 h). Samples shown in these optical images are graphene transferred on Si/SiO$_2$. (**B** and **D**), Schematics illustrating the cross-sectional views of 2LG growth behaviors in Stranski–Krastanov (SK) and Frank-van der Merwe (FM) growth modes, on commercial and treated Cu, respectively. (**E**) Bottom, pixel counts as a function of gray values, for an original microscopy (OM) image of typical SK- and FM-mode grown graphene film, respectively. Top, statistical labelling for each layer of graphene. Both samples were grown for 1h. (**F**) Bottom, optical images of a typical graphene grown with 3.33 h, for both SK and FM modes. Top, occurrence probability for different graphene layers that was statistically identified using the method shown in E, with 20 typical optical images, with sizes of at most 40×40 µm$_2$, taken from both SK- and FM-mode grown samples (10 each). Multilayer graphene (MLG) represents 3LG, 4LG, and above. The occurrence probability of 1LG in these samples are not shown, they are 2.64% and 0.29% for SK mode and FM mode respectively. All scale bars are 5 µm.
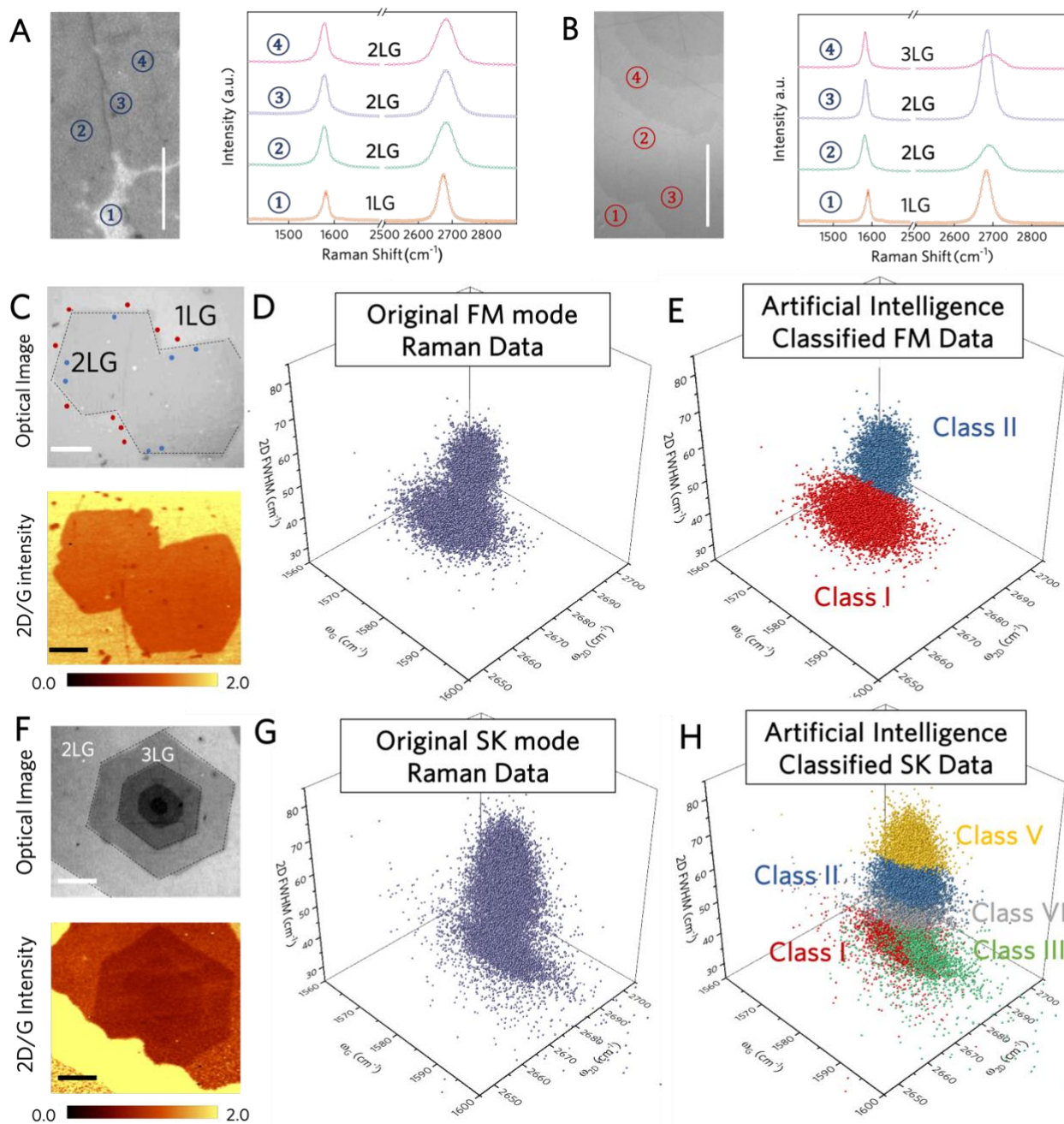
15

Fig. 3. Raman analysis of graphene samples grown via FM and SK mode. (**A**) Optical image of a typical FM-mode grown 2LG sample and the corresponding Raman spectra taken at different positions as indicated. (**B**) Optical image of a typical SK-mode grown 2LG sample and the corresponding Raman spectra taken at different positions as indicated. (**C**) Optical image of a typical FM-mode grown sample with two merging 2LG domains and the corresponding Raman map of I$_{2D}$/I$_G$. (**D**) 3D plot of the G band position (ω_G), 2D band position (ω_{2D}), and 2D band's full width at half maximum (2D FWHM), extracted from 18,000 Raman spectra of the FM-mode grown sample. (**E**) 3D plot showing artificial-intelligence-classified data: Class I (red) and II (blue), which can be identified as the Raman data of 1LG and 2LG, respectively. Manual verification of Raman data at the boundary between Class I and II were conducted at 15 locations marked as red (Class I) and blue (Class II) dots in Fig. 3C

and S3, respectively. (**F**) Optical image of a typical SK-mode grown graphene with islands of thicker graphene and the corresponding Raman map of I2D/IG. (**G**) 3D plot of the ω_G, ω_{2D}, and 2D FWHM, extracted from 20,250 Raman spectra of the SK-mode grown sample. (**H**) 3D plot showing artificial-intelligence-classified data: Class I (red), II (blue), III (light green), IV (grey), and V (yellow), which can be identified as the Raman data of 1LG, quasi-AB-stacked 2LG, larger-twisting-angle 2LG, 3LG, and MLG respectively. All scale bars are 5 μm.
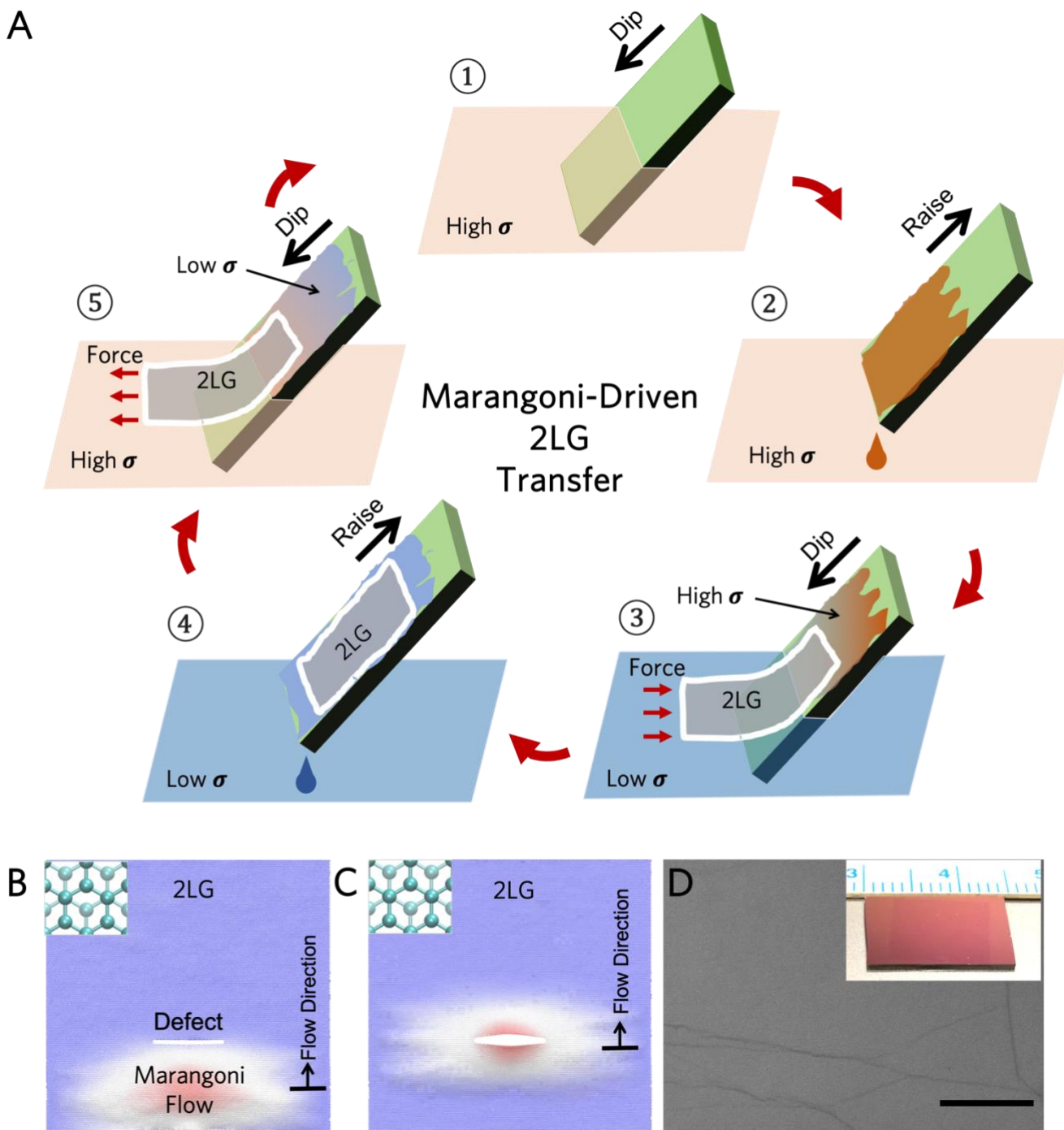
Fig. 4. Support-free 2LG graphene transfer driven by Marangoni effect. (**A**) Schematics showing the concept of our Marangoni-driven graphene transfer process. A graphene sample was first floated on a liquid (either Cu etchant or DI water). A flat scoop (*e.g.* wafer or glass slide) was wetted with a liquid of higher surface tension (high-σ) and immediately dip into the container with graphene sample. Driven by Marangoni flow, the graphene will automatically climb to the flat scoop. Once the flat scoop was brought back to the high-σ liquid, the graphene sample gradually glides from the flat scoop and stays on the liquid surface. (**B** to **C**) Snapshots of a simulated Marangoni flow passing through a 2LG film (see Movie S2). The 2LG remains robust under the Marangoni flow, even in the presence of atomic defects. Insets: Atomic structures of an AB-stacked 2LG used in the molecular

dynamic simulation. (**D**) SEM image of a typical 2LG sample transferred on a Si/SiO$_2$ substrate by our support-free Marangoni-driven approach. Inserted figure: optical image demonstrating centimeter-scale transfer capability of the support-free Marangoni-driven transfer. Scale bar is 20 μm.